REPORT DOCUMENTATION PAGE

Form Approved
OMB No. 0704-0188

(2)

AD-A232 886

Report Date.	3. Report Type and Dates Covered.
1990	Journal Article

Nonlinear propagation in an ocean acoustic waveguide

5. Funding Numbers.

Program Element No. 990101
Project No. 0101
Task No. TTT
Accession No. DN258097

6. Author(s).

John J. Ambrosiano, Daniel R. Plante, B. Edward McDonald, and W. A. Kuperman

7. Performing Organization Name(s) and Address(es).

Ocean Sciences Directorate
Naval Oceanographic and Atmospheric Research Laboratory
Stennis Space Center, MS 39529-5004

8. Performing Organization Report Number.

JA 322:055:89

9. Sponsoring/Monitoring Agency Name(s) and Address(es).

Sandia National Laboratory
Albuquerque, NM 87185

10. Sponsoring/Monitoring Agency Report Number.

JA 322:055:89

11. Supplementary Notes.

JASA

Original contains color plates: All DTIC reproductions will be in black and white

12a. Distribution/Availability Statement.

Approved for public release; distribution is unlimited.

12b. Distribution Code.

13. Abstract *(Maximum 200 words).*

The nonlinear progressive wave equation (NPE) is used to investigate propagation of acoustic pulses in a shallow ocean waveguide. The nonlinearity is shown to affect transmission and reflection at a fluid-fluid interface. It is shown that one effect of the nonlinearity is to reduce the critical angle for total internal reflection from that of the linear case. When loss versus range for a simple isovelocity waveguide is compared with linear normal mode and parabolic equation calculations, the nonlinear result shows increased transmission loss as long as the wave amplitude is significant (an expected result of shock processes), and increased bottom penetration. Nonlinear aging of the waveform alters the excitation of linear modes in the farfield.

14. Subject Terms.	15. Number of Pages.
(U) Nonlinear Propagation; (U) Shock Waves; (U) Acoustics	9
	16. Price Code.

17. Security Classification of Report.	18. Security Classification of This Page.	19. Security Classification of Abstract.	20. Limitation of Abstract.
Unclassified	Unclassified	Unclassified	SAR

NSN 7540-01-280-5500

Standard Form 298 (Rev. 2-89)
Prescribed by ANSI Std. 239-18
298-102

Nonlinear propagation in an ocean acoustic waveguide

John J. Ambrosiano and Daniel R. Plante
Berkeley Research Assoc., Box 852, Springfield, Virginia 22150

B. Edward McDonald[a)]
Naval Ocean R&D Activity, Stennis Space Center, Mississippi 39529

W. A. Kuperman
Naval Research Laboratory, Washington, DC 20375

(Received 11 October 1988; accepted for publication 3 October 1989)

The nonlinear progressive wave equation (NPE) is used to investigate propagation of acoustic pulses in a shallow ocean waveguide. The nonlinearity is shown to affect transmission and reflection at a fluid–fluid interface. It is shown that one effect of the nonlinearity is to reduce the critical angle for total internal reflection from that of the linear case. When loss versus range for a simple isovelocity waveguide is compared with linear normal mode and parabolic equation calculations, the nonlinear result shows increased transmission loss as long as the wave amplitude is significant (an expected result of shock processes), and increased bottom penetration. Nonlinear aging of the waveform alters the excitation of linear modes in the farfield.

PACS numbers: 43.25.Cb, 43.25.Jh, 43.30.Qd

INTRODUCTION

The nonlinear progressive wave equation (NPE) model[1] has recently been developed to investigate nonlinear acoustic effects (including shocks). The model is cast in the time domain as the most economical method for representing local nonlinear phenomena. For investigating propagation in an ocean waveguide, this model provides an alternative to the parabolic equation (PE) and normal mode (NM) approaches.

The NPE is derived from the fluid equations of momentum and mass continuity retaining lowest-order nonlinearity and assuming propagation within a narrow angle. The model follows a pulse disturbance in a reference frame that moves at a constant representative sound speed c_0 in the range direction (x). The local *linear* sound speed in the medium is $c = c_0 + c_1(x,y,z)$ where c_1 is a small local environmental departure from c_0. Consistent with the PE, the NPE can be derived from an ordering scheme in which smallness of various items is formally stated through a scaling variable ϵ. In addition to the PE's list of small quantities, the NPE scales the wave amplitude by ϵ. The list of scaled items precedes Eq. (2). The NPE[1] is stated as

$$\frac{DR}{Dt} = -\frac{\partial}{\partial x}\left(c_1 R + \frac{\beta c_0}{2} R^2\right) - \frac{c_0}{2}\int_{x_f}^{x} \nabla_1^2 R\, dx + O(\epsilon^3), \tag{1}$$

where $R = \rho'/\rho_0$ with ρ' the acoustic density fluctuation and ρ_0 is the ambient density (assumed constant here) in the medium. The coefficient of nonlinearity is $\beta \equiv 1 + \partial \log c/\partial \log \rho \simeq 3.5$ for the ocean. The lower limit x_f of integration in (1) is located in the quiescent medium ahead of the wave. On the right-hand side of Eq. (1), the c_1 term represents refraction, the quadratic term contains nonlinear steepening, and the integral term includes diffraction and geometric spreading.

The error term in (1) is third-order in the smallness parameter ϵ, which scales each of $\{R, c_1, \nabla_1^2, D/Dt\}$, where the last two items of the list are the transverse Laplacian and the wave's time derivative in the wave-tracking frame:

$$\frac{D}{Dt} = \frac{\partial}{\partial t} + c_0 \frac{\partial}{\partial x}. \tag{2}$$

The scaling of D/Dt in this context is not an arbitrary assignment, but a fundamental result from the equations of motion.[1] This is illustrated by the limit $\epsilon \to 0$, which brings $\{c_1, R, \nabla_1^2\}$ to zero on the right side of (1). The appropriate progressive wave solution is a linear plane wave in a homogeneous medium, $f(x - c_0 t)$, with f an arbitrary function. For any solution of this form, D/Dt vanishes, consistent with it being scaled by ϵ.

The equivalence of the NPE and PE under appropriate circumstances has been demonstrated elsewhere.[1,2] As with the PE, any term in (1) contributes meaningfully to wave evolution only as long as it exceeds the dominant error term.

One can reformulate the NPE in terms of a dimensionless pressure variable $Q \equiv p'/\rho_0 c_0^2$:

$$\frac{DQ}{Dt} = -\frac{\partial}{\partial x}\left(c_1 Q + \frac{\beta c_0}{2} Q^2\right) - \frac{c_0}{2}\int_{x_f}^{x} \nabla_1^2 Q\, dx + O(\epsilon^3). \tag{3}$$

One recognizes (3) as differing from (1) only in the substitution of Q for R. The reason for this symmetry is that $Q = R + O(\epsilon^2)$. Substitution of this expression into (3) leads to an error of order ϵ^3 in each term, consistent with (1). The pressure formulation of the NPE (3) facilitates the handling of interfacial boundary conditions.

[a)] Present address: Naval Research Laboratory, Washington, DC 20375.

 0001-4966/90/041473-09$00.80

In the following sections, we present solutions of the NPE for a pulse propagating along an acoustic waveguide descriptive of a shallow ocean. We will show how nonlinearity affects transmission and reflection at the bottom (represented by a fluid–fluid interface) and dispersion in the waveguide. Viscosity and sedimentary attenuation in the ocean and bottom are omitted for simplicity (there is, however, a wave-absorbing buffer zone below to prevent artificial grid reflections). The physical effects to be investigated here are not substantially altered by either of these dissipative mechanisms. Linear results from our model ($\beta = 0$) compare well with existing linear results. Effects evident when nonlinearity is included are physically understandable. Thus two necessary conditions are fulfilled to argue that the NPE is suitable for more complicated investigations as well.

I. SIMULATIONS OF REFLECTION AND TRANSMISSION AT A FLUID–FLUID INTERFACE

In this section, we present results of simulations using the pressure interpretation of the NPE (3). We consider a fluid–fluid description[3] of the ocean–bottom interface as in Fig. 1. The linear sound speed of the water column is c_0 and that of the flat bottom is $c_b = c_0 + c_1$, with $c_1 > 0$. Results are calculated in a reference frame moving at the water sound speed c_0, beginning with conditions illustrated in Fig. 2 (more details below). The subbottom has the same properties as the bottom, plus wave-absorbing numerical attenuation. Azimuthal symmetry is assumed.

Before giving the numerical results, we will present a simple theoretical argument indicating how nonlinearity should affect total internal reflection at the ocean–bottom interface. From simple kinematics, we can derive an expression for the critical grazing angle α_c below which an incident nonlinear plane wave in the ocean fails to excite a nonevanescent wave in the bottom. At the critical grazing angle, the incoming wave barely excites a horizontally propagating wave deep in the bottom. Without having to solve for nonlinear details at the interface, a necessary condition for excitation of the wave deep in the bottom is matching of horizontal phase speeds (i.e., a statement of Snell's law). For this matching, we need a steady-state incoming plane wave. The only such wave with small but finite amplitude is a weak shock discontinuity. Mathematically, this wave consists of two constant states $Q = 0$ ahead of the shock, and $Q = Q_s > 0$ behind it. Within the compressed fluid behind the shock, sound waves propagate at an increased speed

$$c_{nl} = c_0(1 + \beta Q_s) + O(\epsilon^2), \tag{4}$$

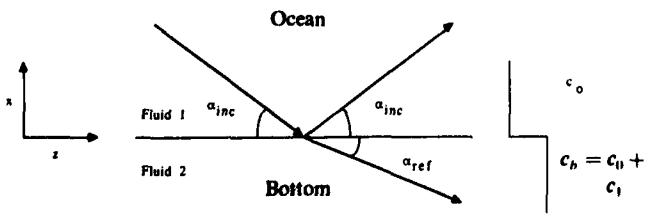

FIG. 1. Plane-wave incident from ocean to bottom, with $c_0 < c_b$. Here, c_0 is the sound speed in the water, c_b is the sound speed in the bottom, α_{inc} is the grazing angle of incidence (reflection), and α_{ref} is the angle of refraction.

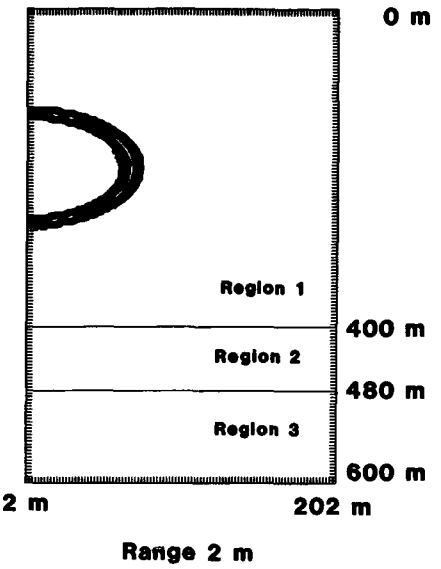

FIG. 2. Simulation window with initial waveform. The ocean and bottom are fluids of equal density with sound speeds of 1500 and 1600 m/s, respectively. The subbottom has the same properties as the bottom, plus numerical damping to absorb waves reflected from the bottom of the numerical grid. The width of the simulation window is 200 m.

where subscript *nl* indicates nonlinear modification. The shock front propagation speed (normal to the front) is given by the Rankine–Hugoniot relation as the average of small signal speeds on both sides of the shock, i.e.,

$$v_s = c_0(1 + \tfrac{1}{2}\beta Q_s) + O(\epsilon^2). \tag{5}$$

The horizontal phase speed of this wave is $v_s \sec \alpha_c$. For this nonlinear problem, we define a critical angle α_c such that the incident wave excites a disturbance in the bottom, which, with increasing depth, approaches a horizontally propagating linear wave with phase speed $c_0 + c_1$. Waves with smaller phase speeds are evanescent in the bottom. The critical grazing angle is thus given by

$$c_0 + c_1 = c_0 \sec \alpha_c(1 + \tfrac{1}{2}\beta Q_s). \tag{6}$$

For small Q_s and c_1/c_0, (6) gives

$$\alpha_c^2 \simeq 2(c_1/c_0) - \beta Q_s. \tag{7}$$

This indicates a decrease of critical angle with the amplitude of the incident wave. Thus, a nonlinear wave might be expected to disturb the bottom more than linear theory would predict. In agreement with this, note that for $Q_s > 0$ and $c_1 < \beta c_0 Q_s/2$, there is no real α_c (no cutoff angle for the nonlinear wave). The sound-speed discontinuity is weak enough that the nonlinear wave passes through to great depth for all grazing angles, while a linear wave would be cut off at $\alpha_c^2 \simeq 2(c_1/c_0)$.

Boundary conditions for the numerical simulations are as follows. The ocean surface is taken to be a flat pressure release surface. The lower boundary of the numerical simulation grid (600-m depth in Fig. 2) is a hard wall $\partial_z = 0$, with reflected waves suppressed by a thick subbottom containing numerical attenuation to be described below. Conditions that must be satisfied at the ocean–bottom interface (400-m depth in Fig. 2) are continuity of fluid pressure and normal particle speed. In terms of the pressure variable Q

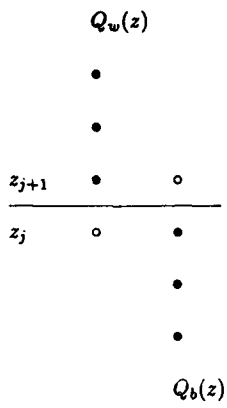

FIG. 3. The fluid–fluid ocean–bottom interface is taken to be midway between two vertical grid points. Auxiliary values for finite differences at the interface (open circles) are generated from the interface continuity conditions (9).

(normalized on *both* sides of the interface by the bulk modulus of *water*, $\rho_0 c_0^2$), the conditions are continuity of Q and $\rho^{-1}\partial_n Q$, where ∂_n is the derivative along the upward normal to the surface.

One finite amplitude effect to be included is deformation of the interface by the wave. To lowest order the slope of the interface deformation ζ is

$$\zeta_x = -\partial_x \int dt \int dt' \rho^{-1} \partial_z p'$$

$$= -\int_{x_j} \partial_z Q \, dx + O(\epsilon^2).$$

The deformation of the surface normal contributes a nonlinear term to the pressure continuity condition for the vertical direction:

$$\rho_{0_w}^{-1} \partial_z Q_w = \rho_{0_b}^{-1} \partial_z Q_b - (\rho_{0_w}^{-1} - \rho_{0_b}^{-1}) \partial_x Q_b \times \int_{x_j} \partial_z Q_b \, dx + O(\epsilon^{\frac{7}{2}}), \tag{8}$$

where subscripts w and b refer to evaluation on the water and bottom side of the interface, respectively. The fractional order in the error term reflects that the NPE scales the transverse Laplacian as ϵ, so that transverse derivatives, e.g., ∂_z, scale as $\epsilon^{1/2}$.

The interfacial boundary conditions are represented numerically as follows. The undisturbed interface is taken halfway between two vertical grid points z_j and z_{j+1} (Fig. 3). The vertical grid may be thought of as partitioned between water and bottom variables Q_w and Q_b. Artificial values Q_{w_j} and $Q_{b_{j+1}}$ are generated from the interfacial boundary conditions. In this work, we examine effects of a sound-speed discontinuity across the interface without the nonlinear boundary term in (8). In the results presented here, we take uniform density across the interface, $\rho_{0_b} = \rho_{0_w}$, so the nonlinear term in (8) is automatically absent. But even allowing a reasonable density discontinuity, neglect of the nonlinear term would be justified by its smallness, estimated as follows. If $\rho_{0_b} = 1.5\rho_{0_w}$, and Q_s is always less than 0.04 (as will be the case considered below when the wave first hits the interface), the nonlinear term on the right side of (8) is initially less than 1% of the linear term, and this ratio decreases with range. Unlike the nonlinearity in (3), its effect does not accumulate during propagation. Retention of the term would affect results considerably less than the uncertainty in real ocean bottom density values. Neglecting the nonlinear term, the second-order finite difference statement of the boundary conditions is

$$Q_{w_j} + Q_{w_{j+1}} = Q_{b_j} + Q_{b_{j+1}},$$
$$\rho_{0_b}^{-1}(Q_{b_{j+1}} - Q_{b_j}) = \rho_{0_w}^{-1}(Q_{w_{j+1}} - Q_{w_j}). \tag{9}$$

Equation (9) allows the artificial values Q_{w_j} and $Q_{b_{j+1}}$ to be eliminated in terms of the active gridpoint values. This representation of the interface conditions is physically consistent with the property that when there is no density discontinuity across the interface, the interface is completely transparent (i.e., $Q_{w_j} = Q_{b_j}$ and $Q_{b_{j+1}} = Q_{w_{j+1}}$).

Equation (3) is integrated in time numerically[1] using Crank–Nicholson for the diffraction term and flux corrected transport (FCT) methods[4–7] for the x derivative. The interfacial boundary conditions are included in the tridiagonal matrix solution for the Crank–Nicholson scheme.

Beneath the bottom, a damping zone is used to absorb downward propagating waves that would otherwise reflect from the bottom of the grid and re-enter the simulation. Damping of unwanted reflections is achieved by the addition of a term $-Q/\tau$ to the right-hand side of Eq. (3), where the purely numerical damping coefficient τ varies with depth.

To study internal reflection at the interface, we initialized a pressure perturbation in the water column and allowed it to propagate to the bottom. We considered two cases: $\beta = 0$ (linear) and $\beta = 3.5$, where the latter is an approximate value for the coefficient of nonlinearity in water. The nonlinear solutions we present do not include the effects of cavitation.

The initial configuration and parameters of the simulations are detailed as follows. The ambient fluid density is taken to be uniform across the interface. The initial pressure perturbation used in both linear and nonlinear simulations is shown in Fig. 2. The perturbation Q is a spherical wave with maximum value $Q = 0.1$ at a radius of 135 m centered about a source point at a depth of 200 m. The wave's radial profile is a half sine wave of width 16 m. A pressure perturbation of this magnitude (but not of this shape) may be expected from an underwater explosion. The shape of the wave automatically relaxes towards an appropriate self-similar profile during propagation.[8] The range variable is x, and depth is in the negative z direction. The grid consists of 100 by 150 points, with spacing $\delta x = 2$ m and $\delta z = 4$ m. We assume a sound speed $c_0 = 1500$ m/s in the ocean and $c_b = 1600$ m/s in both the bottom and damping regions. The linear critical grazing angle ($Q_s = 0$) from (6) is 20 deg. The timestep is initially 0.01 s and is thereafter adjusted to be no greater than half that allowed by the Courant–Friedrichs–Lewy (CFL) stability condition.[9]

Some discussion of the starting field of Fig. 2 is in order. The NPE, like the PE, is a small-angle approximation; yet the starting field contains large-angle components with respect to the range direction. The feature of the NPE that allows accurate recovery of farfield results is that the large-angle wave components have group velocities less than that of the advancing simulation window (less by a factor of the cosine of the propagation angle). These components pro-

gressively fall behind the field of view and do not affect the farfield results.

Simulations results are shown in color in Fig. 4, beginning when the maximum propagation angle has dropped to 25 deg (vertical scale compression by a factor of 3 appears to increase this angle). Pressure perturbations in linear [4(a)–(c)] and nonlinear [4(d)–(f)] cases are pictured at fixed times for comparable values of range (defined as the distance from the source point to the left of the simulation grid). The range values do not match exactly because the timesteps are automatically adjusted during the runs. The color scale from blue to red differs from plot to plot. Reddish hues (yellow

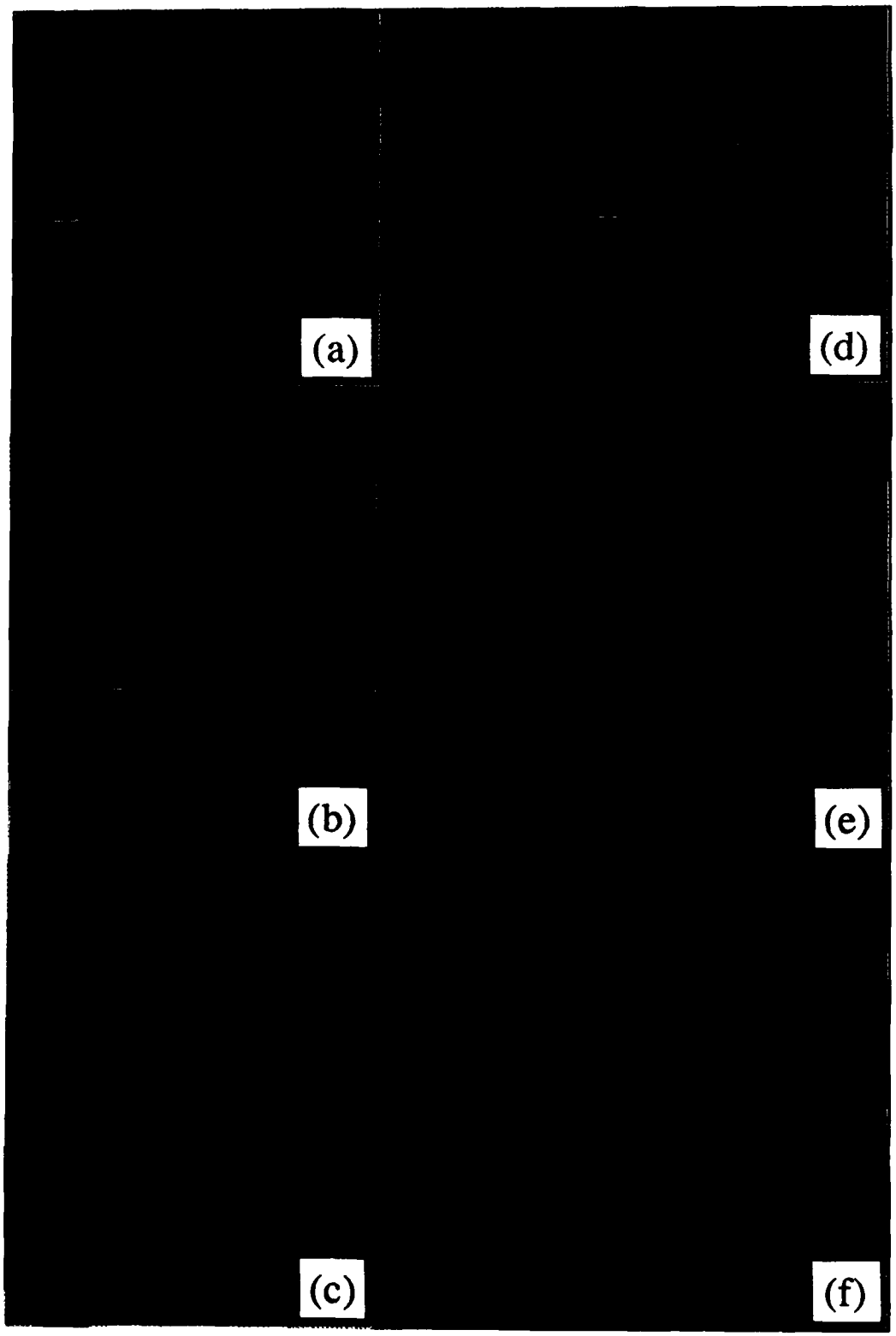

FIG. 4. Color contour plots of propagating pulse at fixed times in pulse following window. Yellow through red are positive, blue–green through violet are negative, and green is neutral (zero). Linear solution is given in (a)–(c); nonlinear solution in (d)–(f). Distances from the source point to the left of each plot are: (a) 452 m, (b) 1352 m, (c) 2252 m, (d) 430 m, (e) 1338 m, and (f) 2207 m.

through red) are always positive, bluish hues (blue–green through violet) are negative, and green is zero. The white horizontal line through the simulation region is the bottom. As the wave propagates far from the source, the effective grazing angle with the bottom becomes approximately inversely proportional to range. In this regard, our results at increasing range show effects of decreasing grazing angle.

Figure 4(a) and (d) is constructed from simulation data at 452 and 430 m, respectively, with (a) being linear and (d) nonlinear. The linear wave intersects the bottom at a grazing angle of approximately 25 deg. Since the linear critical grazing angle is 20 deg, energy can still propagate into the bottom for a short while. An obvious difference between the two cases is the shape of the waveforms. The propagating wave in the linear case maintains its essential half-sine wave profile, while the nonlinear wave has steepened into a shock ahead of what appears to be an exponential tail.

Figure 4(b) and (e) shows the pressure perturbations at 1352 and 1338 m, respectively. The linear wave's grazing angle with the bottom (approximately 8 deg) is now well below critical, and propagation into the bottom has been cut off. The nonlinear wave continues to propagate as a sharp front, while the linear wave maintains a rounded profile. At this range, the bottom-reflected linear wave is a positive pulse followed by a negative pulse of approximately equal amplitude. The nonlinear wave has a predominantly positive reflection. There is a local maximum in linear and nonlinear waves near the bottom evident as a red area. Comparing the shape and size of this region reveals that much of the nonlinear wave's energy resides in the bottom-reflected wave, while the linear wave's energy is primarily in the direct arrival. This is a result of the nonlinear direct arrival being weakened by shock processes, rather than a strengthening of the reflected wave. (The color plot automatically rescales each frame to minimum and maximum values for clarity of presentation.)

Figure 4(b) and (e) shows the transient behavior of the energy that penetrated the bottom earlier in the wave's evolution. This energy appears as a finger somewhat ahead of the main wave. Separation from the wave occurs when the grazing angle goes subcritical. From this point on, additional energy does not radiate into the bottom, but runs ahead and radiates back into the water column (this is evident from movies made in a similar calculation). Energy diagnostics (not shown here) confirm that despite the nonlinear wave's weakening by shock processes, it has deposited more energy into the bottom by this time than the linear wave. We interpret this as being due to a smaller critical angle for the nonlinear wave, and discussed above.

Finally, we compare the two cases at 2252 and 2207 m downrange, as seen in Fig. 4(c) and (f), respectively. Disturbance of the bottom by the linear wave (c) is negligible, while the nonlinear wave (f) still shows some disturbance. The bottom reflection of the linear wave has shifted in phase and become mostly negative, as predicted by linear theory. This leads to destructive interference at and below the interface. The nonlinear reflected wave, however, is still substantially positive, resulting in constructive interference with the direct arrival (this mechanism for increased bottom disturbance is separate from the nonlinear decrease in the critical angle). Another physical effect visible in Fig. 4 is that the nonlinear wave propagates slightly faster than the linear wave. By the time of Fig. 4(c) and (f), the forward edge of the nonlinear wave has crept forward relative to the coordinate system moving at speed c_0, while that of the linear wave has remained fixed.

The above comparison can be summarized as follows. A linear compressional wave incident on a fluid–fluid interface undergoes a transition from positive to negative reflection as the effective grazing angle drops below the critical value and tends to zero. When nonlinear effects are included, the critical angle is smaller, the reflected wave is primarily positive, the disturbance of the bottom is greater, and pulse propagation is slightly faster.

II. DISPERSION OF A WAVE PACKET

A. Normal modes

The results of the previous section suggest that large-amplitude waves, such as those resulting from an underwater explosion, will interact differently with the ocean–bottom interface than small-amplitude waves, because of the nonlinear contribution to the local sound speed. Because of this effect, we expect the dispersion of a nonlinear pulse to be different than in the linear case. In this section, we present numerical results using the NPE model designed to highlight some of those differences.

We consider an idealized shallow ocean like that pictured in Fig. 2. In this case, we assume an ocean depth of 200 m together with 200 m of bottom, the lower four-fifths of which is progressively damped to avoid numerical reflection from the lower simulation boundary. At a source depth of 50 m, we initialize a five-cycle sine-wave packet with a wavelength consistent with a frequency of 50 Hz and limit the angular spread to 38 deg. A Gaussian envelope of $1/e$ width 1.77 cycles multiplies the sine-wave packet. The sound speed in the water column is taken to be 1500 m/s and, in the bottom, is 1550 m/s. The initial perturbation is then allowed to propagate downrange.

Data from a simulated array of 15 hydrophones placed at various downrange locations are stored during the run as a collection of time series. We ran a linear case ($\beta = 0$) out to 20 km and repeated the simulation for a nonlinear case ($\beta = 3.5$). An initial amplitude $Q_{\max} = 0.2$ was chosen to illustrate differences between linear and nonlinear propagation.

Normal mode solutions ϕ to the wave equation for a harmonic point source of a single frequency at depth z_0 (for the case of azimuthal symmetry) are

$$\phi(r,z) = \frac{i}{4}\rho(z_0)\sum_n u_n(z_0)u_n(z)H_0^{(1)}(k_n r), \qquad (10)$$

where $\rho(z_0)$ is the density at the source depth z_0 and $H_0^{(1)}$ is the Hankel function of the first kind. The normal modes $u_n(z)$ are eigenfunctions of the equation

$$d^2u_n(z)/dz^2 + [k^2(z) - k_n^2]u_n(z) = 0. \qquad (11)$$

In Eq. (11), $k(z) = \omega/c(z)$ is the wavenumber and k_n^2 is the eigenvalue for mode n. The normal modes propagate at

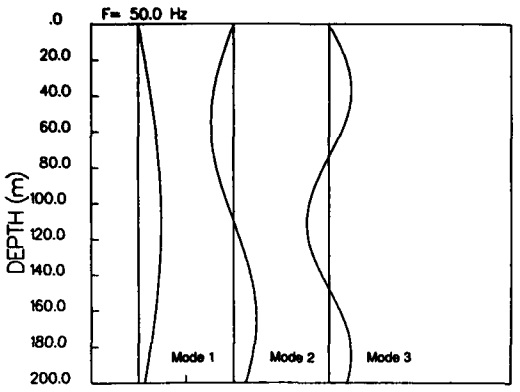

FIG. 5. Normal mode solution from SNAP. The three modes are shown.

different speeds and will separate as the pulse propagates downrange. The normal modes of the waveguide have been calculated numerically[10] and results are depicted in Fig. 5.

Figure 6 shows simulated hydrophone time-series plotted as a function of reduced time using the NPE model for the linear case. Reduced time is defined for each vertical array relative to the time at which the pulse first arrives at the hydrophone array. Figure 6(a) shows the readings at a range of 600 m, and clearly there is no mode separation. Figure 6(b) shows the readings for the hydrophone array at 5 km downrange. At this distance, the mode separation is incomplete, although there is some indication of modes two and three splitting away from the packet. Further downrange at 20 km, the modes have separated, as seen in Fig. 6(c). The dashed lines in Fig. 6(c) indicate approximate arrival times of normal mode maxima. We can see that the general appearance of the modes is consistent with the predictions of normal mode analysis. For example, in the second mode arrival [reduced time 0.20 to 0.25 s in Fig. 6(c)] a phase reversal is evident along the vertical dashed lines, with a null at approximately 108-m depth. Figure 6(d) shows the amplitudes at each of the dashed-line arrival times as a function of hydrophone depth.

The simulated hydrophone data in the nonlinear case reveal differences from the linear results. Figure 7(a) shows these results for a range of 600 m. The most apparent difference is the wave steepening. The individual waveforms are also more complex. Even though the presence of nonlinearity does not allow the rigorous mathematical extraction of normal modes, we expect similarity between the cases since the nonlinearities considered here are weak. After an initial phase in which the nonlinear wave loses energy to shock processes and increased bottom penetration, its interaction with the waveguide becomes essentially linear.

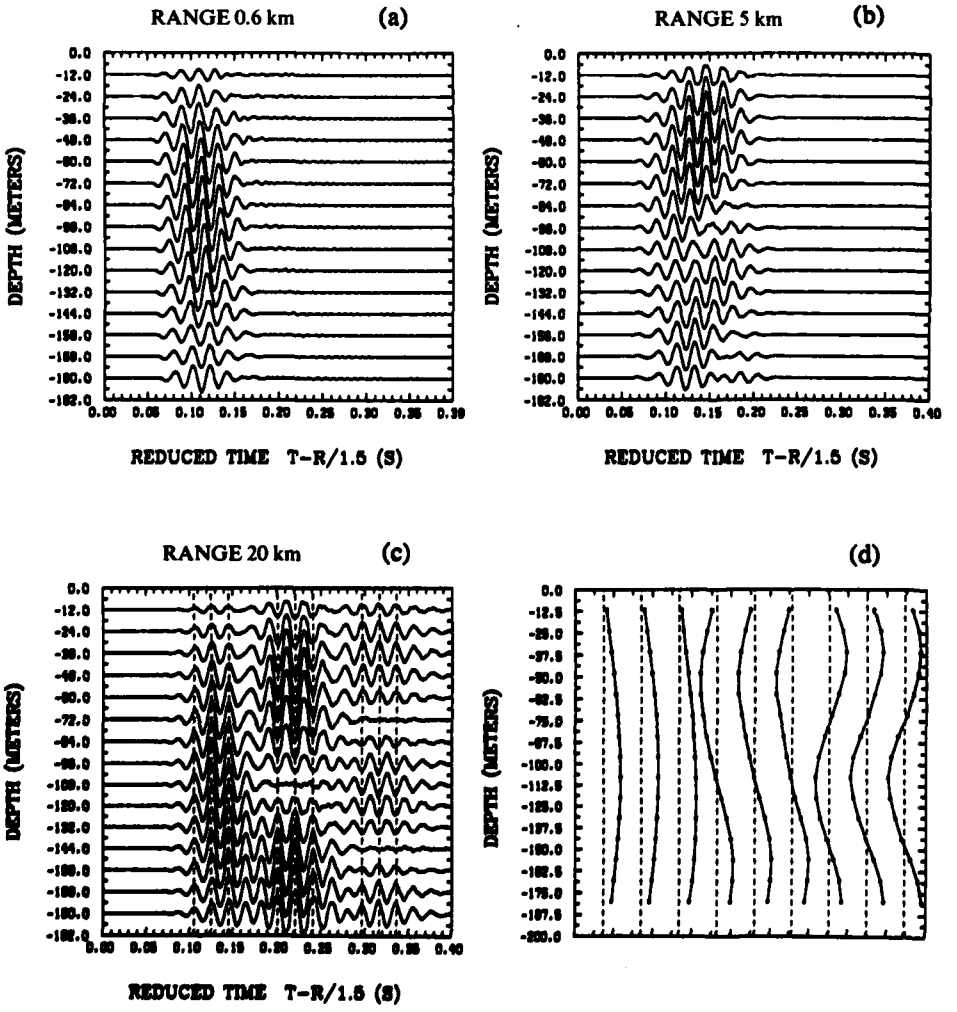

FIG. 6. Numerically simulated hydrophone readings at ranges of (a) 600 m, (b) 5 km, and (c) 20 km for the linear case. In (c), the nine vertical lines are used to point out the mode structure of the simulated hydrophone data. At a range of 20 km, there is a clear separation of the modes. In (d), the modes marked in (c) are displayed.

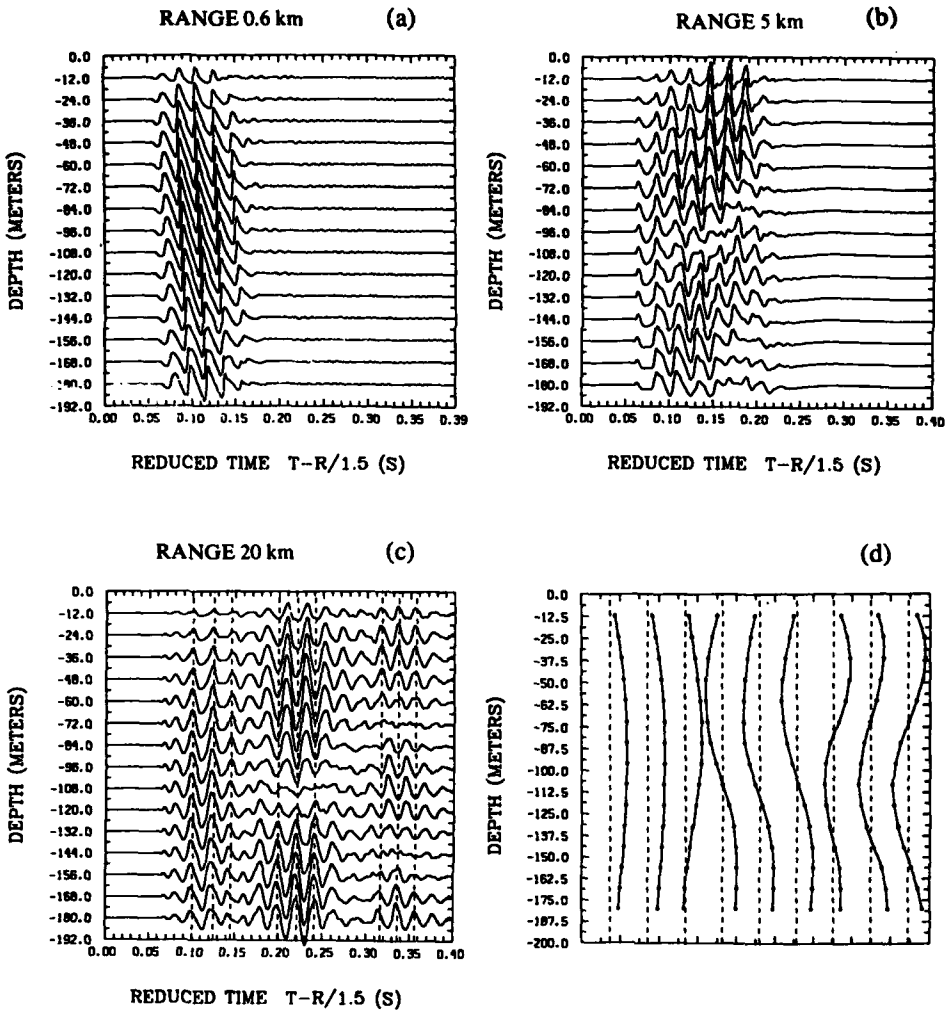

FIG. 7. Nonlinear case for the same conditions as Fig. 6.

With these points in mind, we examine the hydrophone data from the simulation of the nonlinear wave shown in Fig. 7(c) at 20 km downrange. Although the results differ from Fig. 6(c), we can make out the arrival of the three "modes" as indicated by the dashed lines. Plotting the hydrophone signal amplitude along the dashed lines yields Fig. 7(d). Again there is relatively good agreement between these modes and the results in Fig. 5. An exception is mode 1 identified in the first three dashed lines of Fig. 7(c) and plotted in (d). While the mode profile in the linear case agrees favorably with that of Fig. 5, the nonlinear profiles are different, exhibiting an amplitude maximum at a depth of about 80 m rather than the deeper 110 m predicted by normal mode analysis. Since these slices in depth are taken near the front of the propagating signal, this departure from the linear result may be an indication of higher early bottom losses in the nonlinear case as compared to the linear case.

The results of the normal mode comparison can be summarized as follows. Agreement is good between the eigenmodes predicted by linear theory and the separate arrivals that emerge during propagation of a wave packet in the linear NPE calculation. In the nonlinear case, time series of the amplitude sampled near the source depth at a relatively short distance downrange exhibit the steepening expected of a weak shock wave. As the nonlinear pulse propagates, the combined effects of shock dissipation and more efficient coupling with the bottom reduce the amplitude relative to the linear wave. Far downrange, dispersion begins to separate the wave into normal modes recognizable from linear theory. The differences that persist between linear and nonlinear cases are evidence of nonlinear aging.[11] (A nonlinear wave propagating in a nondispersive medium undergoes changes in its profile and in the shape of its frequency spectrum. These changes are "remembered" when the wave weakens enough to be considered linear.)

B. Frequency spectra

In the previous section, we examined normal modes of the waveguide by sampling time series from vertical arrays of points at several well-separated locations downrange. Fourier analysis of time series at the source depth yields information about changes in the frequency spectrum with range.

Figure 8 shows frequency spectra for the simulations of Sec. II A at specific locations downrange for the linear case. Throughout the range from 600 m to 20 km, the spectrum remains strongly peaked near the initial central frequency of 50 Hz. The Gaussian envelope has its peak at 0 Hz and along with the 50-Hz, five-cycle sine wave forms harmonics at 50-Hz intervals (i.e., 100, 150, 200 Hz, etc.).

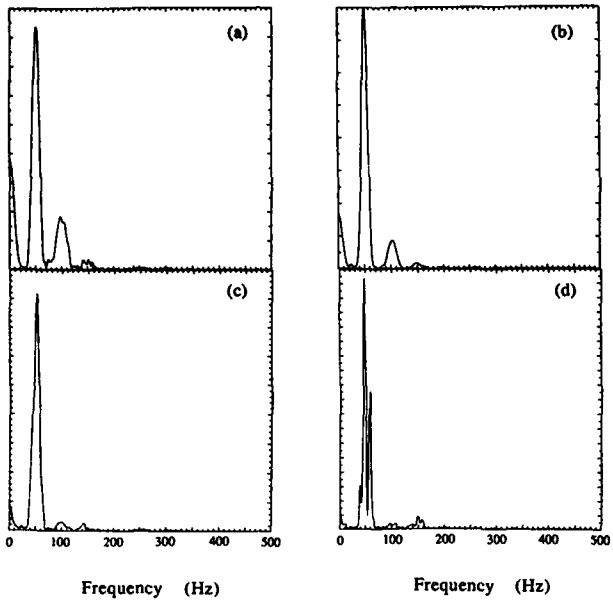

FIG. 8. Spectrum of propagating pulse at ranges (a) 600 m, (b) 5 km, (c) 10 km, and (d) 20 km. The pulse used is a five-cycle sine wave multiplied by a Gaussian envelope.

Figure 9, depicting the nonlinear results, presents a striking contrast. While the predominant frequency remains near 50 Hz, the sidelobes containing other frequencies are of considerably greater amplitude than in the linear case, particularly at the short range of 600 m. This is the stage at which the wave steepens into a shock, giving rise to high-frequency components. As the wave continues to propagate, the composition of frequencies changes and begins more closely to resemble the linear case.

C. Loss versus range

In this section, we examine loss versus range for a single frequency, benchmarking the NPE against standard linear techniques in the linear regime. We also compare the nonlinear case with linear predictions.

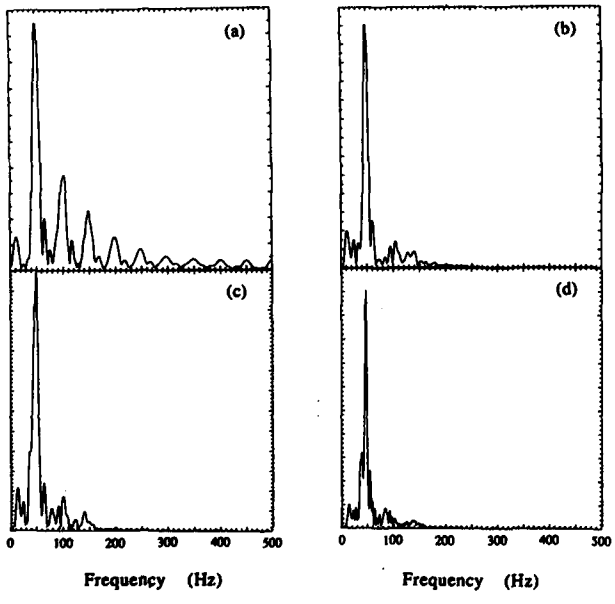

FIG. 9. Nonlinear case for the same conditions as Fig. 8.

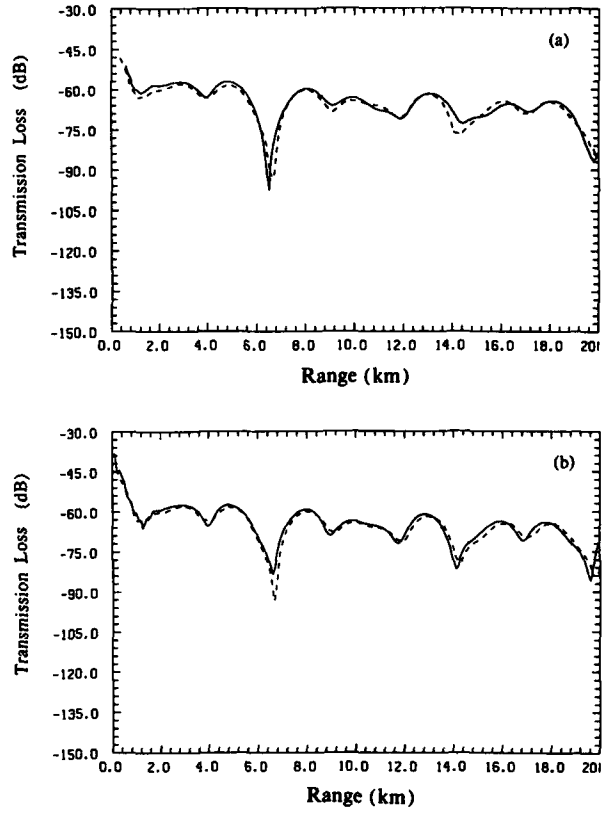

FIG. 10. Loss versus range for the linear simulations. (a) The NPE ($\beta = 0$) (solid) versus the normal-mode (dashed) calculations, while (b) shows the PE (solid) versus the normal-mode (dashed) calculations. Both agree favorably with the normal-mode solution.

The 50-Hz spectral component from Sec. II B is plotted against range in Fig. 10. Shown here are the NPE versus the normal mode solutions [in Fig. 10(a)] and the PE results from the PAREQ model[12] versus the normal mode solutions [in Fig. 10(b)]. We see that both the NPE and PE models are in good agreement with the normal mode predictions.

Figure 11 is a comparison of losses between the linear normal mode solution and the NPE results, including nonlinearity. There is a substantial initial loss of energy that we attribute to shock processes and to increased bottom penetration. Later, the losses parallel those in the linear case.

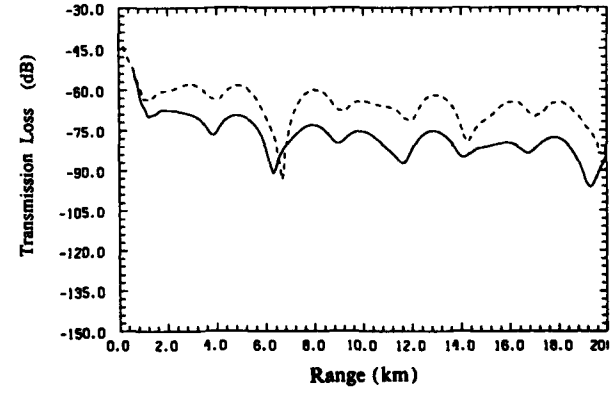

FIG. 11. Loss versus range comparing the nonlinear ($\beta = 3.5$, $Q_{max} = 0.2$) NPE calculation (solid line) with the linear normal-mode result (dashed line).

III. SUMMARY AND CONCLUSION

We have used the NPE model to compare linear and nonlinear acoustic propagation in a shallow-water waveguide. Nonlinear effects evident in the comparison are: (1) a smaller critical grazing angle at the bottom, resulting in enhanced transmission of wave energy; (2) energy loss near the source attributed to shock formation; and (3) nonlinear aging evident in differences in normal-mode excitation as the wave weakens. In its linear mode, the NPE was compared with parabolic equation and normal-mode methods. Transmission loss versus range from all three are in good agreement.

Using simulated data from sample points arranged as hydrophone arrays, we have been able to identify eigenmodes of the waveguide and compare them with normal-mode results. In the linear case, the simulated profiles agree with mode predictions. In the nonlinear case, differences are evident, although similarities with the linear eigenmodes are identifiable. Of the three nonlinearly distorted modes, the first two exhibit some departure from the calculated linear modes and appear to peak nearer the surface. An example of a nonlinear mode that agrees with the linear result is also evident. This is consistent with the idea that the nonlinear pulse loses a large amount of energy to shock processes and to increased bottom penetration (lower critical angle). After the initial nonlinear reduction in wave amplitude, the signal propagates and disperses in a manner similar to the linear case. Differences that persist after the wave weakens [Figs. 6(c) and (d) vs 7(c) and (d)] are attributed to nonlinear aging of the wave.

Data from sample points were also Fourier analyzed to obtain frequency spectra during propagation. There are strong differences shown in this analysis between linear and nonlinear waves. The steepening of the shock front is evident in the generation of high-frequency components. The resulting spectrum downrange is much broader than for the corresponding linear case, and the central frequency is also lower.

Finally, the consistency of our linear results with the existing literature, taken together with the physical plausibility of our nonlinear results, lends credibility to the NPE as a suitable numerical/theoretical tool for studying nonlinear acoustic phenomena.

ACKNOWLEDGMENTS

This work was supported by the Naval Ocean Research and Development Activity and Sandia National Laboratory.

[1]B. E. McDonald and W. A. Kuperman, "Time Domain Formulation for Pulse Propagation Including Nonlinear Behavior at a Caustic," J. Acoust. Soc. Am. **81**, 1406 (1987).
[2]B. E. McDonald and W. A. Kuperman, "Time-Domain Solution of the Parabolic Equation Including Nonlinearity," Comput. Math. Appl. **11**, 843 (1985).
[3]D. R. Plante, J. J. Ambrosiano, and B. E. McDonald, "Compressional Waves at Fluid–Fluid Interface: Transition to Total Internal Reflection," *Advances in Computer Methods for Partial Differential Equations—VI*, edited by R. Vichnevetsky and R. S. Stepleman (IMACS, Rutgers University, New Brunswick, NJ, 1987).
[4]J. P. Boris and D. L. Book, "Flux-Corrected Transport I: SHASTA—A Fluid Transport Algorithm that Works," J. Comput. Phys. **11**, 38 (1973).
[5]S. T. Zalesak, "Fully Multidimensional Flux—Corrected Transport Algorithms for Fluids," J. Comput. Phys. **31**, 335 (1979).
[6]B. E. McDonald, "Flux Corrected Pseudospectral Method for Scalar Hyperbolic Laws," J. Comput. Phys. **82**, 413 (1989).
[7]B. E. McDonald and J. Ambrosiano, "High Order Upwind Flux Methods for Scalar Hyperbolic Conservation Laws," J. Comput. Phys. **56**, 448 (1984).
[8]B. E. McDonald, "Similarity Solution for Low Mach Number Spherical Shocks," J. Acoust. Soc. Am. **84**, 1497 (1988).
[9]R. D. Richtmyer and K. W. Morton, *Difference Methods for Initial Value Problems* (Wiley, New York, 1967), p. 323.
[10]F. B. Jensen and M. C. Ferla, "SNAP: the SACLANTCEN Normal-mode Acoustic Propagation Model," SACLANTCEN Rep. SM-121 (SACLANT ASW Research Center, La Spezia, Italy, 1979).
[11]R. Beyer, *Nonlinear Acoustics* (Naval Sea Systems Command, Arlington, VA, 1974), pp. 124 and 143.
[12]F. B. Jensen and M. G. Martinelli, "The SACLANTCEN Parabolic Equation Model (PAREQ)," SACLANT Report (La Spezia, Italy, SACLANT ASW Research Center, 1985).

Reprinted from:
THE JOURNAL OF THE ACOUSTICAL SOCIETY OF AMERICA **VOL. 87, NO. 4, APRIL 1990**